

**A comparison of global heat flow interpolation
techniques**

Buchanan C. Kerswell¹Matthew J. Kohn¹

¹Department of Geosciences, Boise State University, Boise, ID 83725

Key Points:

-
-
-

9 **Abstract**

10 **## Loading libraries**

11 **1 Introduction**

12 Heat escaping the solid Earth's surface indicates a dynamically cooling planet. Surface heat flow databases (Hasterok & Chapman, 2008; Luazeau, 2019; Pollack et al., 1993) provide a way to understand geodynamics by relating the amount of heat escaping Earth's surface to heat-transferring and heat-generating subsurface processes such as diffusion, hydrothermal circulation, radioactive decay, fault motion, subduction dynamics, and mantle convection (Currie et al., 2004; Currie & Hyndman, 2006; Fourier, 1827; Furlong & Chapman, 2013; Furukawa, 1993; Gao & Wang, 2014; Hasterok, 2013; Kerswell et al., 2020; Parsons & Sclater, 1977; Pollack & Chapman, 1977; Rudnick et al., 1998; Stein & Stein, 1992, 1994; Wada & Wang, 2009). Surface heat flow observations continue to motivate research, evident by more than 1,393 publications compiled in the most recent heat flow dataset, although the rate of publications using surface heat flow has declined since the mid 1980's (Jennings & Hasterok, 2021).

24 Many research questions, such as calculating the global surface heat flux from continents and oceans, require interpolating discrete heat flow observations onto a continuous approximation of Earth's surface. Previous attempts at interpolation use one or more geographic, geologic, geochronologic, or geophysical proxies to predict heat flow at unknown locations by association with similar observation sites (e.g., bathymetry or elevation, proximity to active or ancient orogens, seafloor age, upper mantle shear wave velocities, Chapman & Pollack, 1975; Davies, 2013; Goutorbe et al., 2011; Lee & Uyeda, 1965; Luazeau, 2019; Sclater & Francheteau, 1970; Shapiro & Ritzwoller, 2004). These methods are called *similarity methods* (Figure 1). The success of such interpolations are typically evaluated statistically by the misfit between the predicted and observed heat flow. However, even statistically-successful heat flow interpolations are difficult to interpret and show unexpected anomalies (Luazeau, 2019). The fidelity and usefulness of interpolations depend on the question being asked and the choice of methodology.

37 Predicting surface heat flow by association with physical proxies is arguably the most reasonable approach to interpolation for global investigations. Our understanding

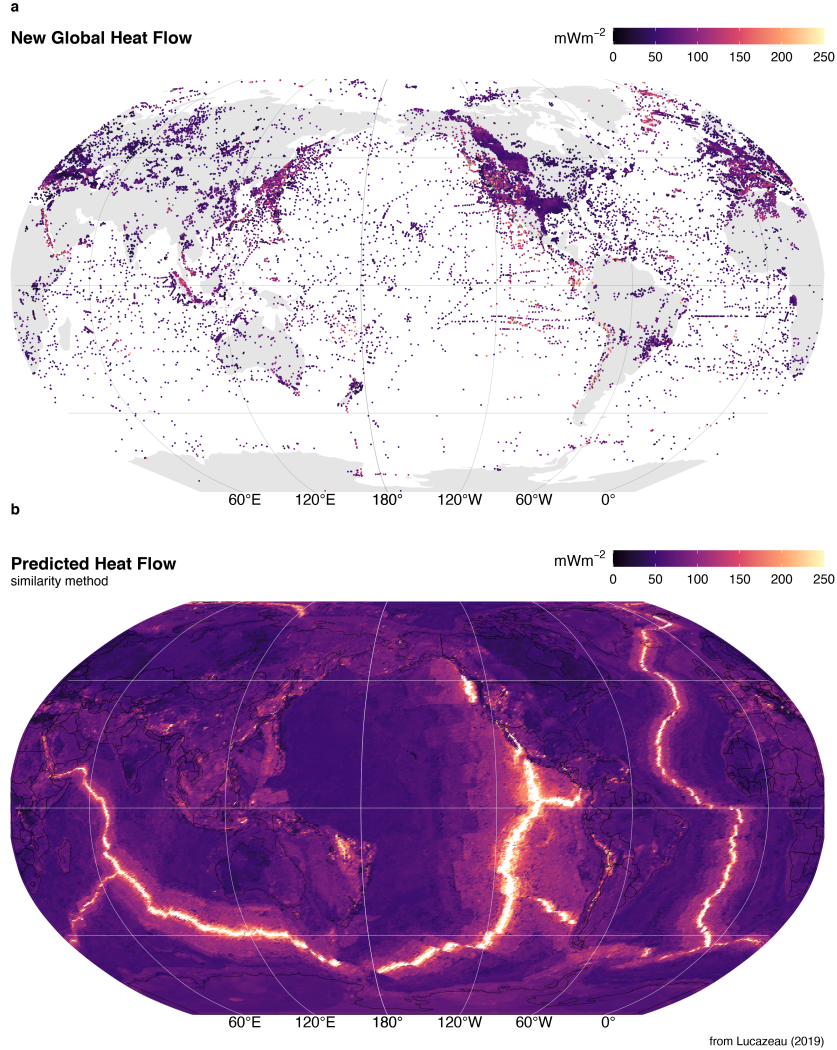


Figure 1: The NGHF dataset. (a) The complete dataset ($n = 69729$), and (b) interpolation by similarity method from Lucaleau (2019).

of geodynamics and near-surface heat flow perturbations implies that the variance in surface heat flow is not uniformly stochastic, but rather, in large part, determined by the physical conditions and processes operating locally (e.g., Goutorbe et al., 2011). For example, younger oceanic plates should have higher surface heat flow than older plates (Stein & Stein, 1992), subducting oceanic plates will lower surface heat flow near trenches (Fukukawa, 1993), and hydrothermal circulation of seawater can modify heat flow in oceanic crust (Hasterok et al., 2011). Interpolation by association with physical proxies makes reasoned predictions of heat flow based on many independently-tested geodynamic models. However, similarity methods are strongly biased towards such models and risk making determinations where, in fact, surprising results and idiosyncrasies may be found.

49 In contrast, there exists some degree of stationarity, spatial dependence, or con-
50 tinuity, in the distribution of surface heat flow. A pair of surface heat flow observations
51 taken one meter apart will be strongly correlated. The correlation between pairs of ob-
52 servations will likely decrease with increasing distance between the pairs (Goovaerts, 1997).
53 The spatial (dis)continuity of surface heat flow represents the areal extent of geodynamic
54 processes and their interactions. For example, consistent patterns of heat flow near vol-
55 canic arcs are interpreted to reflect common backarc lithospheric thermal structures and
56 slab-mantle mechanical coupling depths in subduction zones (Furukawa, 1993; Kerswell
57 et al., 2020; Wada & Wang, 2009).

58 In theory, one may predict surface heat flow at unknown locations by considering
59 many nearby observations (i.e. Kriging, Krige, 1951). However, Kriging is disadvanta-
60 geous for global interpolations of surface heat flow because it assumes that the under-
61 lying distribution of heat flow is stationary (constant in space), which effectively ignores
62 geodynamic complexity. One can overcome this problem by relaxing assumptions of sta-
63 tionarity, or applying Markov-Bayes techniques to include proxies as priors (Bárdossy,
64 1997). Instead, we leverage the properties of stationarity as a tool for comparison with
65 *similarity* methods of interpolation (Goutorbe et al., 2011; Lucaleau, 2019). So the ques-
66 tions are: 1) What are the differences between Kriging and similarity methods? 2) What
67 are the implications of the differences according to the implicit assumptions in both meth-
68 ods?

69 We attempt to answer these questions by using ordinary Kriging to interpolate the
70 New Global Heat Flow (NGHF) dataset of Lucaleau (2019). Our method is optimized
71 using a genetic algorithm to minimize an objective function which considers both the
72 misfit on the variogram models and interpolation results (after Li et al., 2018). We then
73 compare our interpolation results to those of Lucaleau (2019) and consider the impli-
74 cations of Kriging vs. similarity methods of interpolation. We restrict our comparison
75 to areas near subduction zone segments defined by Syracuse & Abers (2006) for two rea-
76 sons: 1) to provide maps and statistics useful to subduction zone research, and 2) to em-
77 phasize differences and idiosyncrasies in both interpolation approaches in a complex tec-
78 tonic and thermal setting.

79 **2 Methods**

80 **2.1 The NGHF Dataset**

81 The NGHF dataset was downloaded from the supplementary material of Lucaleau
 82 (2019). It contains 69729 data points, their locations in latitude/longitude, and metadata—
 83 including a data quality rank (Code 6) from A to D (with Code 6 = Z = undetermined).
 84 The reader is referred to Lucaleau (2019) for details on compilation, references, and his-
 85 torical perspective on the NGHF and previous compilations. We use NGFH because it
 86 is the most recent dataset available, has been carefully compiled, and is open-access.

87 Like Lucaleau (2019), we exclude 4790 poor quality observations (Code 6 = D) from
 88 our analysis. We further remove 350 data points without heat flow observations and two
 89 without geographic information. Multiple observations at the same location are parsed
 90 to avoid singular covariance matrices during Kriging:

$$\begin{aligned}
 f(X_i^q, Y_i^q) = & \\
 X_i^q > Y_i^q \rightarrow z_i &= x_i \\
 X_i^q < Y_i^q \rightarrow z_i &= y_i \\
 X_i^q = Y_i^q \rightarrow z_i &= RAND(x_i, y_i)
 \end{aligned} \tag{1}$$

91 where X_i^q and Y_i^q represent the quality of each duplicate observation pair at loca-
 92 tion i , $RAND$ is a random function that selects either the observation x_i or y_i , and z_i
 93 stores the observation selected by $f(X_i^q, Y_i^q)$. The final dataset used for Kriging has $n =$
 94 55274 observations after parsing $n = 32430$ duplicate observation.

95 **2.2 Kriging**

96 Kriging is a three-step process that involves first estimating an experimental vari-
 97 iogram, $\hat{\gamma}(h)$, fitting the experimental variogram with one of many variogram models,
 98 $\gamma(h)$, and finally using the modelled variogram to predict random variables at unknown
 99 locations (Cressie, 2015; Krige, 1951). We use the general-purpose functions defined in
 100 the “R” package `gstat` (Gräler et al., 2016; Pebesma, 2004) to perform all three steps.
 101 We begin by estimating an experimental variogram as defined by Bárdossy (1997):

$$\hat{\gamma}(h) = \frac{1}{2N(h)} \sum_{N(h)} (Z(u_i) - Z(u_j))^2 \quad (2)$$

where $N(h)$ is the number of pairs of points, $Z(u_i)$ and $Z(u_j)$, separated by a lag distance, $h = |u_i - u_j|$. We evaluate $\hat{\gamma}(h)$ at fifteen lag distances by binning the irregular spaced data with a bin width, δ , equal to one-third of the maximum lag distance divided by the number of lags used to evaluate the variogram, $\delta = \max(N(h))/(3 \cdot 15)$. Then $N(h) \leftarrow N(h, \delta h) = \{i, j : |u_i - u_j| \in [h - \delta h, h + \delta h]\}$. In simple terms, Equation 2 represents the similarity, or dissimilarity, between pairs of observations in space. Equation 2 is derived from the theory of *regionalized variables* (Matheron, 1963, 2019), which formally defines a probabilistic framework for spatial interpolation of natural phenomena. It is important for the reader to understand the fundamental assumptions implicit in Equation 2 in order to understand the comparison of interpolation techniques discussed later. The basic assumptions used in our Kriging method are:

- $\hat{\gamma}(h)$ is directionally invariant (isotropic)
- $\hat{\gamma}(h)$ is evaluated in two-dimensions and neglects elevation, $Z(u) \in \mathbb{R}^2$
- The first and second moments of $Z(u)$ have the following conditions over the domain D :

$$\begin{aligned} E[Z(u)] &= \text{mean} = \text{constant}, & \forall u \in D \\ E[(Z(u + h) - \text{mean})(Z(u) - \text{mean})] &= C(h), & \forall |u, u + h| \in D \end{aligned} \quad (3)$$

The last assumption (Equation 3) is called “second-order stationarity” and is commonly used in practice. It assumes the underlying probability distribution of the random variable, $Z(u)$, does not change in space and the covariance, $C(h)$, only depends on the distance, h , between two random variables. These assumptions are expected to be valid in cases where the underlying natural process is stochastic, spatially continuous, and has the property of additivity such that $\frac{1}{n} \sum_{i=1}^n Z(u_i)$ has the same meaning as $Z(u)$ (Bárdossy, 1997).

The following are two illustrative cases where Equation 3 is likely valid:

1. The thickness of a sedimentary unit with a homogeneous concentration of radioactive elements can be approximated by $q_s = q_b + \int A dz$, where q_b is a constant heat flux entering the bottom of the layer and A is the heat production within the

layer with thickness z (Furlong & Chapman, 2013). If we have two samples, $Z(u_1) = 31 \text{ mW/m}^2$ and $Z(u_2) = 30.5 \text{ mW/m}^2$, their corresponding thicknesses would be $Z'(u_1) = 1000 \text{ m}$ and $Z'(u_2) = 500 \text{ m}$ for $A = 0.001 \text{ mW/m}^3$ and $q_b = 30 \text{ mW/m}^2$. The variable, $Z(u)$, in this case is additive because the arithmetic mean of the samples is a good approximation of the average sedimentary layer thickness, $(Z(u_1) + Z(u_2))/2 = 750 \text{ m}$.

- 134 2. The age of young oceanic lithosphere can be approximated by $q_s(t) = kT_b(\pi\kappa t)^{-1/2}$,
 135 where $q_s(t)$ is the surface heat flow of a plate with age, t , T_b is the temperature
 136 at the base of the plate, k is thermal conductivity, and $\kappa = k/\rho C_p$ is thermal dif-
 137 fusivity (Stein & Stein, 1992). For $k = 3.138 \text{ W/mK}$, $\rho = 3330 \text{ kg/m}^3$, $C_p =$
 138 1171 J/kgK , $T_b = 1350^\circ\text{C}$, two samples, $Z(u_1) = 180 \text{ mW/m}^2$ and $Z(u_2) =$
 139 190 mW/m^2 , would correspond to plates with ages of $Z'(u_1) = 10 \text{ Ma}$, and $Z'(u_2) =$
 140 9 Ma , respectively. Since $Z(u_1)+Z(u_2)/2 = 185 \text{ mW/m}^2$ and $Z'(185 \text{ mW/m}^2) =$
 141 $9.5 \text{ Ma} = Z'(u_1) + Z'(u_2)/2$, the variable $Z(u)$ in this case is also additive.

142 In contrast, Equation 3 is likely invalid in regions that transition among two or more
 143 tectonic regimes. For example, the expected heat flow $E[Z(u)] = \text{mean}$ will change when
 144 moving from a spreading center to a subduction zone. $E[Z(u)] = \text{mean} \neq \text{constant}$
 145 over the region of interest. Proceeding with Equation 3 in this case has the effect of mask-
 146 ing the geodynamic complexity. In other words, the spatial dependence is considered in
 147 the Kriging method in this case, but the geodynamic structure is *invisible*. We will see
 148 that this has important implications when comparing our Kriging method to Lucaleau
 149 (2019)'s interpolation method, which is exactly opposite of this formalism—it only con-
 150 siders the similarities among physical proxies and not spatial dependence.

151 The second step is to fit the experimental variogram with a variogram model, $\gamma(h)$.
 152 In this study we fit three popular variogram models to the experimental variogram. We
 153 use models with sill, which implies the spatial dependence between pairs of points has
 154 a finite range. The spherical, exponential, and Gaussian variogram models are defined
 155 as (Chiles & Delfiner, 2009; Cressie, 2015):

$$\begin{aligned}
sph \leftarrow \gamma(h) &= \begin{cases} n + s \left(\frac{3h}{2a} - \frac{1}{2} \left(\frac{h}{a} \right)^3 \right), & \text{if } 0 \leq h \leq a \\ n + s, & \text{if } h > a \end{cases} \\
exp \leftarrow \gamma(h) &= n + s \left(1 - \exp \left(\frac{-h}{a} \right) \right), \quad \text{if } h \geq 0 \\
Gau \leftarrow \gamma(h) &= n + s \left(1 - \exp \left(\frac{-h^2}{a^2} \right) \right), \quad \text{if } h \geq 0
\end{aligned} \tag{4}$$

where n is the nugget, s is the sill, and a is the effective range. For spherical, exponential, and Gaussian models, the effective range is related to the range, r , by $a = r$, $a = r/3$, and $a = 1/r\sqrt{3}$, respectively (Gräler et al., 2016; Pebesma, 2004). The function `fit.variogram` in `gstat` allows one to try many variogram models and the best will be selected by the minimum misfit by weighted least square (WLS, Pebesma, 2004).

We use ordinary Kriging for our interpolation step, which predicts the value of a random function, $\hat{Z}(u)$ at unknown locations as a linear combination of all known locations in the domain, D (Bárdossy, 1997):

$$\hat{Z}(u) = \sum_{i=1}^n \lambda_i Z(u_i), \quad \forall u \in D \tag{5}$$

The conditions in Equation 3 set up a constrained minimization problem since one has:

$$E[Z(u)] = mean, \quad \forall u \in D \tag{6}$$

The linear estimator must obey

$$E[\hat{Z}(u)] = \sum_{i=1}^n \lambda_i E[Z(u_i)] = mean \tag{7}$$

so the weights must be:

$$\sum_{i=1}^n \lambda_i = 1 \tag{8}$$

This is the first constraint, also known as the unbiased condition, which states that the sum of the weights must equal one. However, there is an infinite set of real numbers

one could use for the weights, λ_i . Our goal is to find the set of weights in Equation 5 that minimizes the estimation variance. This can be solved with the covariance function, $C(h)$ from Equation 3:

$$\begin{aligned}\sigma^2(u) &= \text{Var}[Z(u) - \hat{Z}(u)] = E \left[(Z(u) - \sum_{i=1}^n \lambda_i Z(u_i))^2 \right] = \\ &E \left[Z(u)^2 + \sum_{j=1}^n \sum_{i=1}^n \lambda_j \lambda_i Z(u_j) Z(u_i) - 2 \sum_{i=1}^n \lambda_i Z(u_i) Z(u) \right] = \\ &C(0) + \sum_{j=1}^n \sum_{i=1}^n \lambda_j \lambda_i C(u_i - u_j) - 2 \sum_{i=1}^n \lambda_i C(u_i - u)\end{aligned}\quad (9)$$

Solving for the weights in Equation 5 with respect to the unbiased condition (Equation 8) and minimum estimate variance (Equation 9), yields the best linear unbiased estimator (BLUE, Bárdossy, 1997). In our case, this is done by the function `krige` in `gstat`.

2.3 Kriging Optimization

Achieving a useful Kriging results depends on one's choice of many Kriging parameters (Θ). In this study, we investigate a set of parameters, Θ :

$$\Theta = \{m, s, a, n, S\} \quad (10)$$

where m is the model type (sph, exp, or Gau), s is the sill, a is the effective range, n is the nugget, and S is the maximum distance for local Kriging. Only points within S from the prediction location are used for Kriging. Our goal is to find Θ such that our interpolation, $f(x_i; \Theta)$, gives the most useful outcome—defined by minimizing a cost function, $C(\Theta)$, that represents the error between the set of real observations, $Z(u_i)$ and predictions, $\hat{Z}(u)$.

We define a cost function that simultaneously considers the misfit between the experimental and modelled variogram and between the Kriging predictions and observed heat flow (after Li et al., 2018):

$$C(\Theta) = (1 - w)C_F(\Theta) + wC_I(\Theta) \quad (11)$$

188 where $C_F(\Theta)$ is the root mean square error (RMSE) of the modelled variogram fit
 189 calculated by WLS, and $C_I(\Theta)$ is the RMSE of the Kriging result calculated by cross-
 190 validation. The weight, w , is set to 0.5 in our study, which balances the effects of $C_F(\Theta)$
 191 and $C_I(\Theta)$ on the cost function. The final expression to minimize becomes:

$$\min(C(\Theta)) = \frac{1-w}{\sigma_E} \sqrt{\frac{1}{N} \sum_{k=1}^N w(h_k)[\hat{\gamma}(h_k) - \gamma(h_k; \Theta)]^2} + \frac{w}{\sigma_S} \sqrt{\frac{1}{M} \sum_{i=1}^M [Z(u_i) - \hat{Z}(u_i; \Theta)]^2} \quad (12)$$

192 where N is the number of pairs of points used to calculate the experimental var-
 193 iogram, $\hat{\gamma}(h_k)$, σ_E is the standard deviation of the experimental variogram, $\hat{\gamma}(h)$, $w(h_k)$
 194 is the weight in WLS and defines the importance of the k th lag in the error estimate.
 195 We use $w(h_k) = N_k/h_k^2$. $Z(u_i)$ and $\hat{Z}(u_i; \Theta)$ are the measured and predicted values,
 196 respectively, σ_s is the standard deviation of the predicted values, $\hat{Z}(u_i)$, and M is the
 197 number of measurements in $Z(u_i)$. For $C_I(\Theta)$ we use ten-fold cross-validation, which splits
 198 the dataset, $|Z(u_i), \forall u_i \in D|$ into ten equal intervals and tests one interval against the
 199 remaining nine. This process is then repeated over all intervals so that the whole dataset
 200 has been cross-validated.

201 Minimization of $C(\Theta)$ is achieved by a genetic algorithm that simulates biologic
 202 natural selection by differential success (Goldberg, 1989). Our procedure is as follows:

- 203 1. Initiate fifty *chromosomes*, ξ , with random starting parameters defined within the
 204 search domain (Table 1)
- 205 2. Evaluate the fitness of each individual chromosome as $-C(\Theta)$ for the entire pop-
 206 ulation
- 207 3. Allow the population to exchange genetic information by sequentially performing
 208 genetic operations:
 - 209 a. Selection: the top 5% fittest chromosomes survive each generation
 - 210 b. Crossover: pairs of chromosomes have an 80% chance of exchanging genetic in-
 211 formation
 - 212 c. Mutation: there is a 10% chance for random genetic mutations
- 213 4. Evaluate the fitness of the new population

- 214 5. If the termination criterion is met, do step (6), otherwise continue to evolve by
 215 repeating steps (3) and (4)
 216 6. Decode the best chromosome and build the optimal variogram

217 We use the general-purpose functions in the “R” package **GA** (Scrucca, 2013, 2016)
 218 to perform each step in the above procedure.

Table 1: Parameters and ranges used in the optimization algorithm

Parameter	Search Domain	Units
Model (m)	[Spherical, Exponential, Guassian]	NA
Sill (s)	[1, 5×10^3]	$(mW/m^2)^2$
Effective Range (a)	[1, 1×10^6]	meters
Nugget (n)	[1, 1×10^3]	meters
Local Search (S)	[1, 1×10^6]	meters

219 2.4 Map Projection and Interpolation Grid

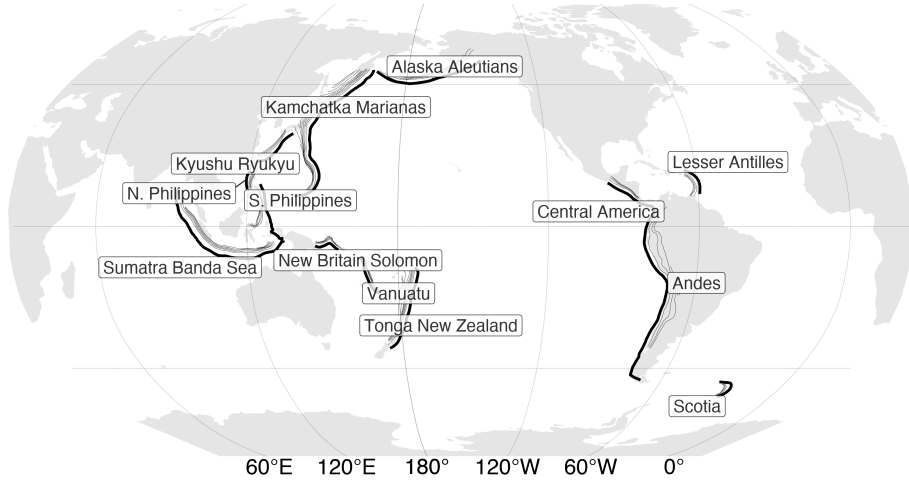
220 We interpolate onto the same $0.5^\circ\text{C} \times 0.5^\circ\text{C}$ grid as Luazeau (2019) so a direct
 221 difference could be calculated between our interpolation methods and Luazeau (2019)’s.
 222 The NGHF and grid with predicted heat flow from Luazeau (2019) were transformed
 223 into a Pacific-centered Robinson coordinate reference system (CRS) defined using the
 224 proj string (PROJ contributors, 2021):

```
225 +proj=robin +lon_0=-155 +lon_wrap=-155 +x_0=0 +y_0=0
226 +ellps=WGS84 +datum=WGS84 +units=m +no_defs
```

227 All geographic operations, including Kriging, are performed in the above CRS us-
 228 ing the general-purpose functions in the “R” package **sf** (Pebesma, 2018). We define the
 229 Kriging domain near individual arc segments in two steps: 1) 1000 km buffers are drawn
 230 around the arc segments as defined by Syracuse & Abers (2006). 2) The bounding box
 231 of the 1000 km buffer is expanded by 10% on all sides (Figure 2). We provide the com-
 232 plete NGHF dataset (Luazeau, 2019), filtered and parsed NGHF dataset, heat flow in-
 233 terpolations (from Luazeau, 2019, and this study), and our code as supplementary in-

234 formation to support FAIR data policy (Wilkinson et al., 2016). These items can also
235 be retrieved from the official repository at <https://doi.org/10.17605/OSF.IO/CA6ZU>.

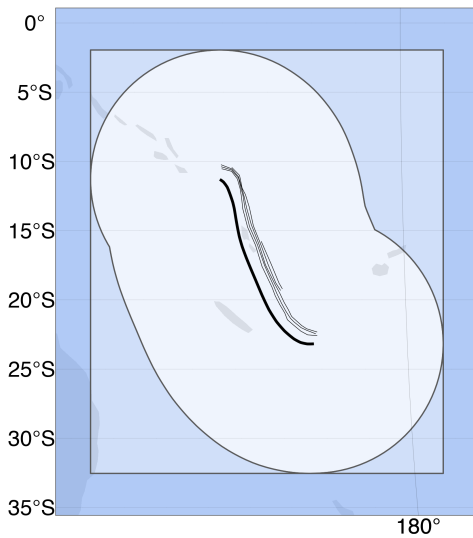
a Subduction Zone Segments



from Syracuse & Abers (2006)

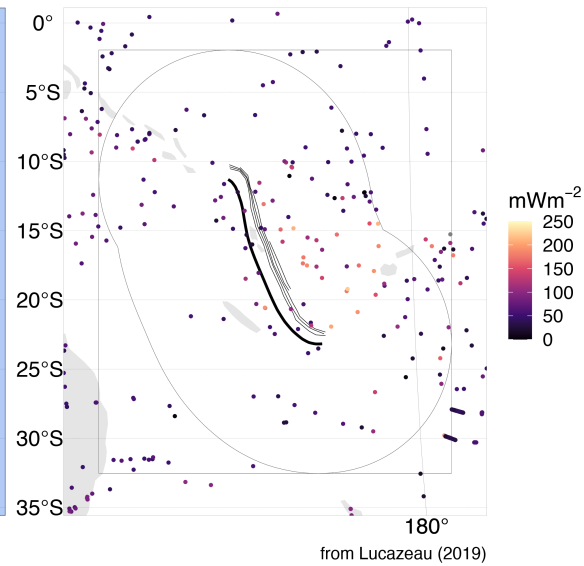
b Vanuatu

Interpolation Domain



c Vanuatu

n = 349



from Lucazeau (2019)

Figure 2: Subduction zone segments and interpolation domain. (a) Heat flow is interpolated around thirteen subduction zone segments by (b) drawing a 1000km buffer (lightest blue) around each segment and expanding the buffer's bounding box (medium blue) by 10% on all sides (darkest blue). (c) The NGHF dataset is cropped within the largest rectangle. Data from Syracuse & Abers (2006) and Lucazeau (2019).

236 **3 Results**237 **3.1 Heat Flow Near Subduction Zone Segments**

238 Summary statistics for surface heat flow observations by subduction zone segment
 239 are given in Table 2 and Figure 3.

Table 2: Summary of heat flow (mWm^{-2}) observations by subduction zone segment

Segment	n	Min	Max	Median	IQR	Mean	Sigma
Alaska Aleutians	2792	4	7765	184	206	233	344
Andes	5226	7	911	45	50	87	88
Central America	5038	8	911	45	48	88	91
Kamchatka Marianas	3956	1	31000	71	48	121	658
Kyushu Ryukyu	3246	1	31000	72	44	130	726
Lesser Antilles	3534	13	1150	41	12	52	50
N. Philippines	1001	3	31000	72	35	206	1276
New Britain Solomon	181	3	174	65	42	69	30
S. Philippines	1442	1	31000	71	43	167	1063
Scotia	72	13	145	76	23	74	28
Sumatra Banda Sea	3037	1	5600	65	47	77	120
Tonga New Zealand	507	1	416	54	40	64	45
Vanuatu	349	1	283	54	40	64	44

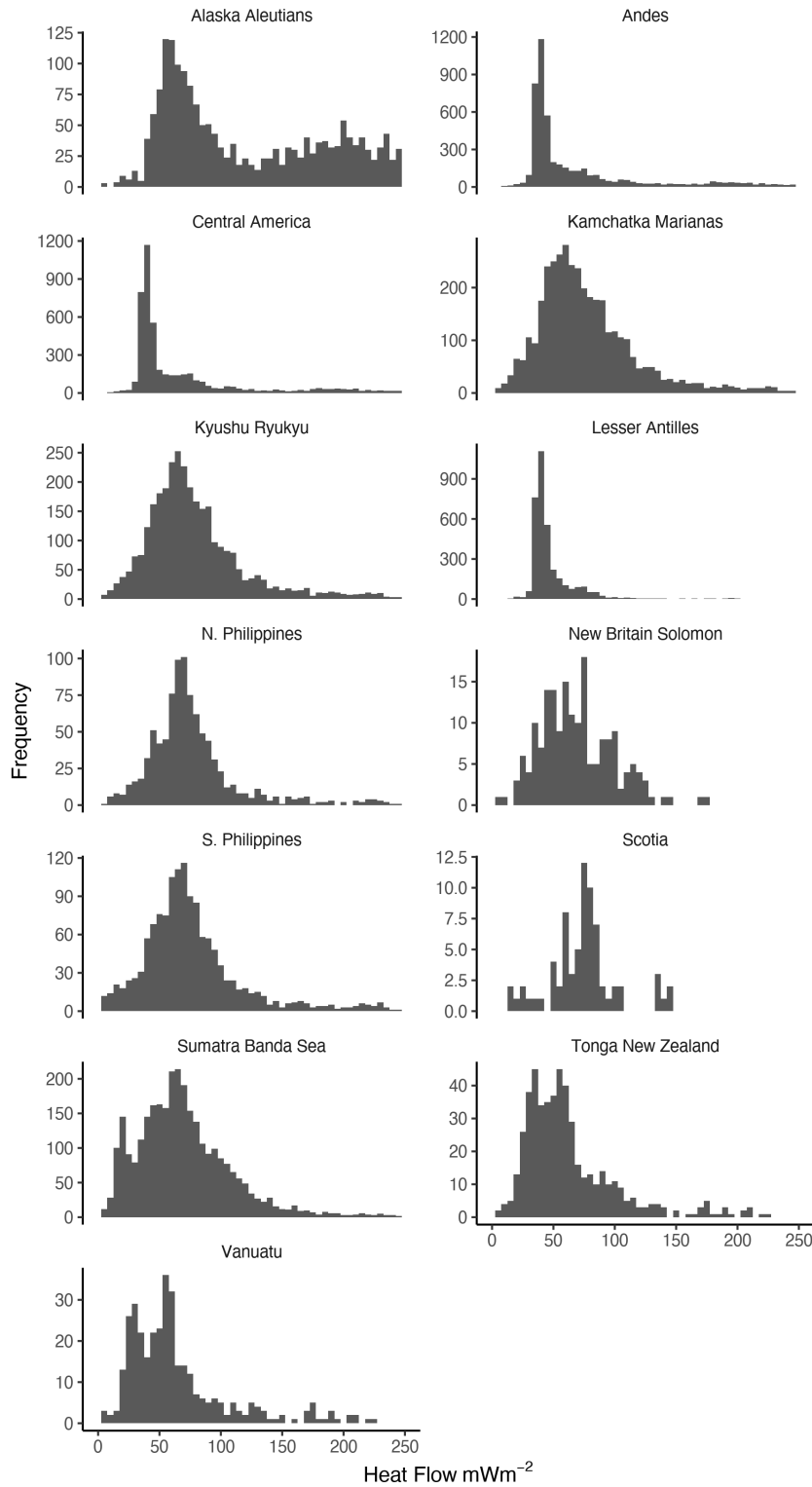


Figure 3: Distribution of heat flow observations by subduction zone segment. Heat flow near most segments are centered around $50\text{ }mWm^{-2}$ and highly skewed right. The skewness likely represents sampling near hydrothermal systems, volcanic arcs, or spreading centers.

²⁴⁰ The optimal variogram models and associated errors $C_F(\Theta)$ and $C_I(\Theta)$ are given
²⁴¹ in Table 3 and Figure 4.

Table 3: Summary of optimal varigram models by subduction zone segment

Segment	Model	Sill	Range
Alaska Aleutians	Exp	3524.0857	117396.66
Andes	Exp	3095.2423	286688.01
Central America	Sph	1747.9487	256703.99
Kamchatka Marianas	Sph	1701.1806	223685.45
Kyushu Ryukyu	Exp	1626.2318	43751.86
Lesser Antilles	Sph	519.1377	89079.02
New Britain Solomon	Exp	816.7801	87822.61
N. Philippines	Sph	1633.3002	31816.29
Sumatra Banda Sea	Exp	1593.4728	140627.05
Scotia	Sph	109.6181	27569.55
S. Philippines	Exp	1705.4852	22516.53
Tonga New Zealand	Exp	1274.7961	82583.96
Vanuatu	Sph	1342.4631	42045.93

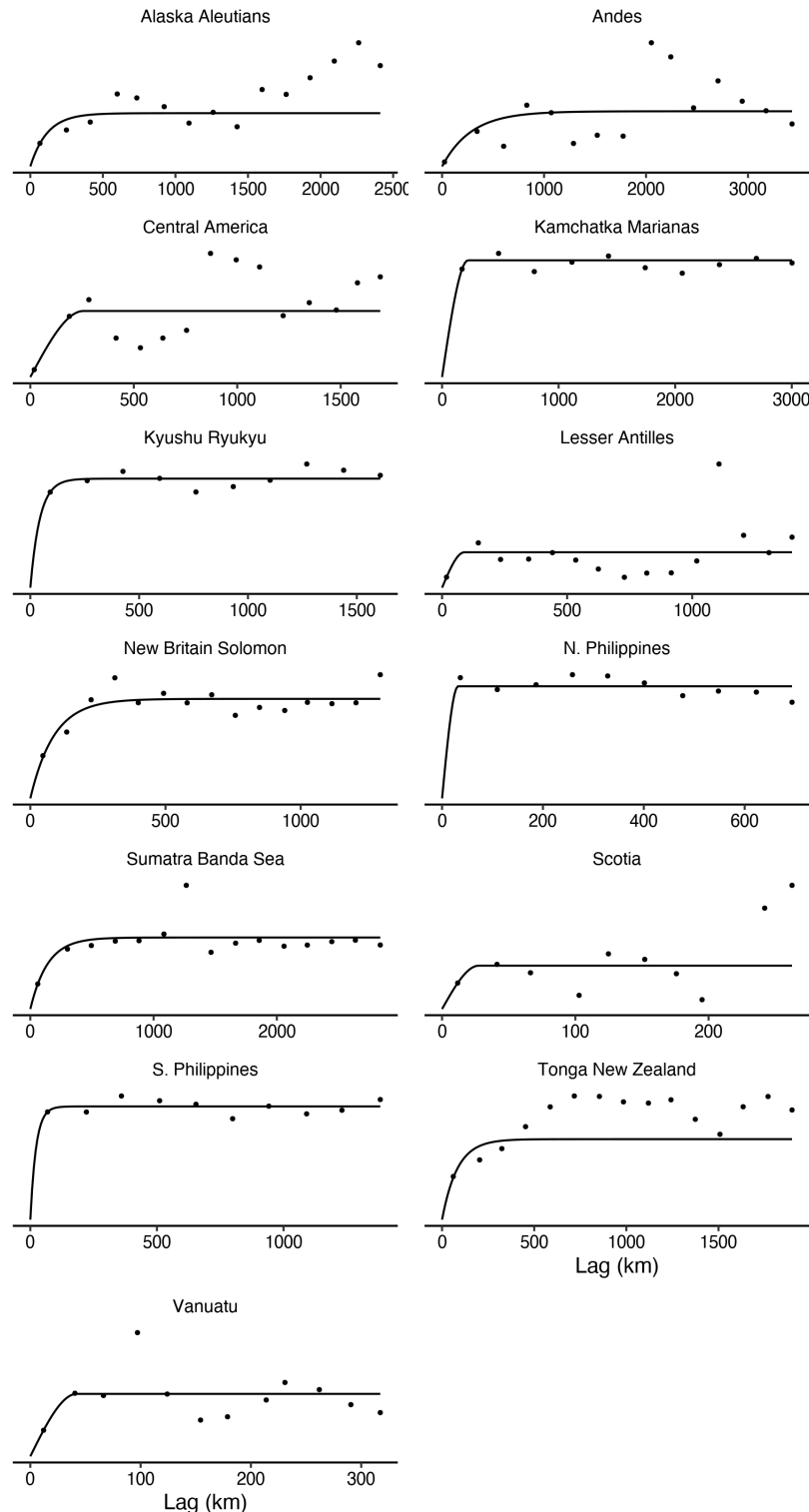


Figure 4: optimal variogram models by subduction zone segment. the y-axis is semivariance (mwm^{-2})². about half of the experimental variograms (dots) deviate, often periodically, from the variogram models. deviations often occur between 500 to 1000 km.

242

Summary statistics for the interpolation differences are given in Table 4.

Table 4: Summary of predicted heat flow differences by subduction zone segment

Segment	Min	Max	Median	IQR	Mean	Sigma
Alaska Aleutians	-169	2784	2	18	7	72
Andes	-122	2313	3	33	13	70
Central America	-119	2777	8	66	49	149
Kamchatka Marianas	-136	305	-1	17	2	17
Kyushu Ryukyu	-101	174	1	21	4	20
Lesser Antilles	-53	666	2	16	12	39
New Britain Solomon	-81	236	2	21	5	20
N. Philippines	-66	296	4	19	7	21
Sumatra Banda Sea	-129	372	2	18	5	19
Scotia	-59	1004	-1	26	8	33
S. Philippines	-79	384	3	24	6	22
Tonga New Zealand	-122	1672	-6	21	1	29
Vanuatu	-88	1701	3	29	7	39

243

4 Discussion

244

5 Conclusions

245

Acknowledgments

246 **References**

- 247 Bárdossy, A. (1997). Introduction to geostatistics. *Institute of Hydraulic Engineering,*
 248 *University of Stuttgart.*
- 249 Chapman, D. S., & Pollack, H. N. (1975). Global heat flow: A new look. *Earth and Plan-*
 250 *etary Science Letters, 28*(1), 23–32.
- 251 Chiles, J.-P., & Delfiner, P. (2009). *Geostatistics: Modeling spatial uncertainty* (Vol. 497).
 252 John Wiley & Sons.
- 253 Cressie, N. (2015). *Statistics for spatial data*. John Wiley & Sons.
- 254 Currie, C., & Hyndman, R. D. (2006). The thermal structure of subduction zone back
 255 arcs. *Journal of Geophysical Research: Solid Earth, 111*(B8).
- 256 Currie, C., Wang, K., Hyndman, R. D., & He, J. (2004). The thermal effects of steady-
 257 state slab-driven mantle flow above a subducting plate: The Cascadia subduction zone
 258 and backarc. *Earth and Planetary Science Letters, 223*(1-2), 35–48.
- 259 Davies, J. H. (2013). Global map of solid earth surface heat flow. *Geochemistry, Geo-*
 260 *physics, Geosystems, 14*(10), 4608–4622.
- 261 Fourier, J. (1827). Mémoire sur les températures du globe terrestre et des espaces planétaires.
 262 *Mémoires de l'Académie Royale Des Sciences de l'Institut de France, 7*, 570–604.
- 263 Furlong, K. P., & Chapman, D. S. (2013). Heat flow, heat generation, and the thermal
 264 state of the lithosphere. *Annual Review of Earth and Planetary Sciences, 41*, 385–
 265 410.
- 266 Furukawa, Y. (1993). Depth of the decoupling plate interface and thermal structure un-
 267 der arcs. *Journal of Geophysical Research: Solid Earth, 98*(B11), 20005–20013.
- 268 Gao, X., & Wang, K. (2014). Strength of stick-slip and creeping subduction megathrusts
 269 from heat flow observations. *Science, 345*(6200), 1038–1041.
- 270 Goldberg, D. E. (1989). Genetic algorithms in search. *Optimization, and MachineLearn-*
 271 *ing.*
- 272 Goovaerts, P. (1997). *Geostatistics for natural resources evaluation*. Oxford University
 273 Press on Demand.

- 274 Goutorbe, B., Poort, J., Lucaleau, F., & Raillard, S. (2011). Global heat flow trends re-
275 solved from multiple geological and geophysical proxies. *Geophysical Journal International*, 187(3), 1405–1419.
- 276
- 277 Gräler, B., Pebesma, E., & Heuvelink, G. (2016). Spatio-temporal interpolation using
278 gstat. *The R Journal*, 8, 204–218. Retrieved from <https://journal.r-project.org/archive/2016/RJ-2016-014/index.html>
- 279
- 280 Hasterok, D. (2013). A heat flow based cooling model for tectonic plates. *Earth and Plan-
281 etary Science Letters*, 361, 34–43.
- 282
- 283 Hasterok, D., & Chapman, D. (2008). Global heat flow: A new database and a new ap-
proach. In *AGU fall meeting abstracts* (Vol. 2008, pp. T21C–1985).
- 284
- 285 Hasterok, D., Chapman, D., & Davis, E. (2011). Oceanic heat flow: Implications for global
heat loss. *Earth and Planetary Science Letters*, 311(3-4), 386–395.
- 286
- 287 Jennings, S., & Hasterok, D. (2021). HeatFlow.org. *Heatflow.org*. Retrieved from <http://heatflow.org/>
- 288
- 289 Kerswell, B. C., Kohn, M. J., & Gerya, T. V. (2020). Backarc lithospheric thickness and
serpentine stability control slab-mantle coupling depths in subduction zones. *Earth
and Space Science Open Archive*, 34. [https://doi.org/10.1002/essoar.10503710
.1](https://doi.org/10.1002/essoar.10503710.1)
- 290
- 291
- 292 Krige, D. G. (1951). A statistical approach to some basic mine valuation problems on
the witwatersrand. *Journal of the Southern African Institute of Mining and Metal-
lurgy*, 52(6), 119–139.
- 293
- 294
- 295 Lee, W. H., & Uyeda, S. (1965). Review of heat flow data. *Terrestrial Heat Flow*, 8, 87–
296 190.
- 297
- 298 Li, Z., Zhang, X., Clarke, K. C., Liu, G., & Zhu, R. (2018). An automatic variogram mod-
eling method with high reliability fitness and estimates. *Computers & Geosciences*,
299 120, 48–59.
- 300
- 301 Lucazeau, F. (2019). Analysis and mapping of an updated terrestrial heat flow data set.
Geochemistry, Geophysics, Geosystems, 20(8), 4001–4024.
- 302 Matheron, G. (1963). Principles of geostatistics. *Economic Geology*, 58(8), 1246–1266.

- 303 Matheron, G. (2019). *Matheron's theory of regionalized variables*. International Asso-
304 ciation for.
- 305 Parsons, B., & Sclater, J. G. (1977). An analysis of the variation of ocean floor bathymetry
306 and heat flow with age. *Journal of Geophysical Research*, 82(5), 803–827.
- 307 Pebesma, E. (2004). Multivariable geostatistics in S: The gstat package. *Computers &*
308 *Geosciences*, 30, 683–691.
- 309 Pebesma, E. (2018). Simple Features for R: Standardized Support for Spatial Vector Data.
310 *The R Journal*, 10(1), 439–446. <https://doi.org/10.32614/RJ-2018-009>
- 311 Pollack, H. N., & Chapman, D. S. (1977). On the regional variation of heat flow, geotherms,
312 and lithospheric thickness. *Tectonophysics*, 38(3-4), 279–296.
- 313 Pollack, H. N., Hurter, S. J., & Johnson, J. R. (1993). Heat flow from the earth's inte-
314 rior: Analysis of the global data set. *Reviews of Geophysics*, 31(3), 267–280.
- 315 PROJ contributors. (2021). *PROJ coordinate transformation software library*. Open Source
316 Geospatial Foundation. Retrieved from <https://proj.org/>
- 317 Rudnick, R. L., McDonough, W. F., & O'Connell, R. J. (1998). Thermal structure, thick-
318 ness and composition of continental lithosphere. *Chemical Geology*, 145(3-4), 395–
319 411.
- 320 Sclater, J. G., & Francheteau, J. (1970). The implications of terrestrial heat flow obser-
321 vations on current tectonic and geochemical models of the crust and upper mantle
322 of the earth. *Geophysical Journal International*, 20(5), 509–542.
- 323 Scrucca, L. (2013). GA: A package for genetic algorithms in r. *Journal of Statistical Soft-
324 ware*, 53(4), 1–37.
- 325 Scrucca, L. (2016). On some extensions to GA package: Hybrid optimisation, parallelisi-
326 sation and islands evolution. *arXiv Preprint arXiv:1605.01931*.
- 327 Shapiro, N. M., & Ritzwoller, M. H. (2004). Inferring surface heat flux distributions guided
328 by a global seismic model: Particular application to antarctica. *Earth and Planetary
329 Science Letters*, 223(1-2), 213–224.
- 330 Stein, C. A., & Stein, S. (1992). A model for the global variation in oceanic depth and
331 heat flow with lithospheric age. *Nature*, 359(6391), 123–129.

- 332 Stein, C. A., & Stein, S. (1994). Constraints on hydrothermal heat flux through the oceanic
333 lithosphere from global heat flow. *Journal of Geophysical Research: Solid Earth*, 99(B2),
334 3081–3095.
- 335 Syracuse, E. M., & Abers, G. A. (2006). Global compilation of variations in slab depth
336 beneath arc volcanoes and implications. *Geochemistry, Geophysics, Geosystems*, 7(5).
- 337 Wada, I., & Wang, K. (2009). Common depth of slab-mantle decoupling: Reconciling
338 diversity and uniformity of subduction zones. *Geochemistry, Geophysics, Geosystems*,
339 10(10).
- 340 Wilkinson, M. D., Dumontier, M., Aalbersberg, Ij. J., Appleton, G., Axton, M., Baak,
341 A., et al. (2016). The FAIR guiding principles for scientific data management and
342 stewardship. *Scientific Data*, 3(1), 1–9.